A DEEP, HIGH-RESOLUTION SURVEY AT 74 MHz

A. S. COHEN,[1,2] H. J. A. RÖTTGERING,[3] M. J. JARVIS,[3,4] N. E. KASSIM,[1] AND T. J. W. LAZIO[1]

ABSTRACT

We present a 74 MHz survey of a 165 deg^2 region located near the north Galactic pole. This survey has an unprecedented combination of both resolution (25″ FWHM) and sensitivity (σ as low as 24 mJy beam^{-1}). We detect 949 sources at the 5 σ level in this region, enough to begin exploring the nature of the 74 MHz source population. We present differential source counts, spectral index measurements, and the size distribution as determined from counterparts in the high-resolution FIRST 1.4 GHz survey. We find a trend of steeper spectral indices for the brighter sources. Further, there is a clear correlation between spectral index and median source size, with the flat spectrum sources being much smaller on average. Ultra-steep spectrum objects ($\alpha \leq -1.2$; $S_\nu \propto \nu^\alpha$) are identified, and we present high-resolution VLA follow-up observations of these sources which, identified at such a low frequency, are excellent candidates for high-redshift radio galaxies.

Subject headings: radio continuum: general — surveys

On-line material: machine-readable table

1. INTRODUCTION

The new 74 MHz system on the Very Large Array (VLA), fully implemented in 1998 (Kassim et al. 1993), has opened a new window into the previously unexplored regime of very low-frequency radio observations at high sensitivity and subarcminute resolution.

The radio source population at very low frequencies is of interest for several reasons. Samples selected at $\nu \sim 74$ MHz are completely dominated by isotropic radio emission, unlike those found at higher frequencies, where orientation-dependent Doppler boosting enhances the observed emission for some fraction of sources: even for the 178 MHz 4C survey (Pilkington & Scott 1965; Gower, Scott, & Wills 1967) 10% of sources were significantly affected by Doppler beaming (Wall & Jackson 1997), leading to biased samples of radio sources where those sources with jets pointing toward us are relatively overrepresented. In addition, at frequencies below 100 MHz spectral curvature is much more common than at higher frequencies, providing an important tool for studying the properties of the absorbing gas. This is because at low frequencies, the needed optical depths for absorption due to free-free absorption by H II regions (intrinsic or intervening) or synchrotron self-absorption require lower electron densities than at higher frequencies.

The ability to find steep spectrum sources is of value because of its relative efficiency in finding very high-redshift radio galaxies ($z > 2$). Identification of ultra-steep spectrum sources has now been used by many groups for a number of years to find the highest redshift radio galaxies (Röttgering et al. 1994; Chambers et al. 1996; Blundell et al. 1998). This method has been implemented mainly with frequencies above

150 MHz (De Breuck et al. 2000; Blundell et al. 1998) and is based on the curved nature of the radio spectral energy distribution. Most low-redshift radio galaxies have spectra that flatten below 325 MHz, while the higher redshift objects are observed at a higher rest frame frequency, where the SED is steep. At 74 MHz, this method is likely to be even more efficient, since the spectra of most low-redshift radio galaxies will have flattened to a much greater degree at this very low frequency, increasing the contrast between them and the high-redshift radio galaxies.

Although radio galaxies are no longer the only galaxies found at the very highest redshifts (Hu et al. 2002; Kodaira et al. 2003; Cuby et al. 2003) and certainly not the most abundant high-redshift galaxies (Steidel et al. 1996, 1999), they do have unique characteristics: (1) the selection via radio emission means that radio-loud active galactic nuclei (AGNs) are selected free of caveats concerning dust, which is probably a very important factor in the high-redshift universe, as is evidenced by the huge submillimeter luminosities associated with radio galaxies at high redshift (e.g., Archibald et al. 2001; Reuland, Röttgering, & van Breugel 2003); (2) their strong narrow emission lines allow relatively simple redshift determinations that do not rely on stellar continuum breaks or absorption lines; and (3) powerful ($L_{151} > 10^{25}$ W m^{-2} Hz^{-1}) radio galaxies inhabit some of the most massive galaxies in the universe at all cosmic epochs (Jarvis et al. 2001; De Breuck et al. 2002; Willott et al. 2003) and as such provide a unique probe into the build-up of massive galaxies. With the recent work on the correlation between black hole mass and bulge luminosity in the local universe (Magorrian et al. 1998), the fact that galaxies which exhibit powerful radio emission are the most massive means they probably host the most massive black holes (Dunlop et al. 2003; Bettoni et al. 2003). The evidence for supermassive black holes in the centers of all bulge dominated galaxies also implies that every massive galaxy in the local universe may have had an active phase in the past. This is further reinforced by the similarity in number density of supermassive black holes in the local universe and the density of quasars at $z \sim 2.5$, i.e., the quasar epoch. Thus, we may need to understand AGN activity to understand massive galaxy formation in general.

[1] Naval Research Laboratory, Remote Sensing Division, Code 7213, Washington, DC 20375; aaron.cohen@nrl.navy.mil, namir.kassim@nrl.navy.mil, joseph.lazio@nrl.navy.mil.

[2] National Research Council Postdoctoral Fellow.

[3] Leiden University, Sterrewacht, Oort Gebouw, P.O. Box 9513, 2300 RA Leiden, Netherlands; rottgeri@strw.leidenuniv.nl.

[4] Astrophysics, Department of Physics, Keble Road, Oxford OX1 3RH, UK; mjj@astro.ox.ac.uk.

Report Documentation Page		*Form Approved* *OMB No. 0704-0188*

Public reporting burden for the collection of information is estimated to average 1 hour per response, including the time for reviewing instructions, searching existing data sources, gathering and maintaining the data needed, and completing and reviewing the collection of information. Send comments regarding this burden estimate or any other aspect of this collection of information, including suggestions for reducing this burden, to Washington Headquarters Services, Directorate for Information Operations and Reports, 1215 Jefferson Davis Highway, Suite 1204, Arlington VA 22202-4302. Respondents should be aware that notwithstanding any other provision of law, no person shall be subject to a penalty for failing to comply with a collection of information if it does not display a currently valid OMB control number.

1. REPORT DATE **FEB 2004**	2. REPORT TYPE	3. DATES COVERED **00-00-2004 to 00-00-2004**
4. TITLE AND SUBTITLE **A Deep, High-Resolution Survey at 74 MHz**		5a. CONTRACT NUMBER
		5b. GRANT NUMBER
		5c. PROGRAM ELEMENT NUMBER
6. AUTHOR(S)		5d. PROJECT NUMBER
		5e. TASK NUMBER
		5f. WORK UNIT NUMBER
7. PERFORMING ORGANIZATION NAME(S) AND ADDRESS(ES) **Naval Research Laboratory,Code 7213,4555 Overlook Avenue, SW,Washington,DC,20375**		8. PERFORMING ORGANIZATION REPORT NUMBER
9. SPONSORING/MONITORING AGENCY NAME(S) AND ADDRESS(ES)		10. SPONSOR/MONITOR'S ACRONYM(S)
		11. SPONSOR/MONITOR'S REPORT NUMBER(S)
12. DISTRIBUTION/AVAILABILITY STATEMENT **Approved for public release; distribution unlimited**		
13. SUPPLEMENTARY NOTES		
14. ABSTRACT		
15. SUBJECT TERMS		

16. SECURITY CLASSIFICATION OF:			17. LIMITATION OF ABSTRACT	18. NUMBER OF PAGES	19a. NAME OF RESPONSIBLE PERSON
a. REPORT **unclassified**	b. ABSTRACT **unclassified**	c. THIS PAGE **unclassified**		**14**	

Standard Form 298 (Rev. 8-98)
Prescribed by ANSI Std Z39-18

A further characteristic of radio galaxies is, by definition, their radio emission. This allows a unique estimate of the time since the radio AGN was triggered (Blundell, Rawlings, & Willott 1999), and it enables us to probe the gaseous environment via Faraday rotation measures (Carilli et al. 1997). But possibly more importantly in the years to come, it allows us to probe 21 cm H I absorption along the line of sight to the radio source. This will be vitally important as 21 cm absorption (and emission) will allow us to probe the epoch of reionization. These studies will be tractable with the development of the new era of radio telescopes such as the LOFAR[5] (Kassim et al. 2000) and the SKA,[6] which will have the sensitivity to probe such a signal. Radio sources that are placed at the epoch before which the reionization is fully completed will be a very important probe of this epoch, allowing the study of the neutral gas at parsec and kiloparsec scales. Such scales are much smaller than those being probed by the *Wilkinson Microwave Anisotropy Probe* or *Planck*. Thus, it is crucial to find radio sources at $z > 6$ to allow these investigations to take place, and selecting ultra-steep spectrum (USS) radio sources is a well proven technique for finding the highest redshift radio galaxies (Rawlings et al. 1996; van Breugel et al. 1999), and selecting at 74 MHz allows us to do this better than ever before.

In this paper, we describe the survey with a discussion of observational methodology in § 2 and the mapping results and source extraction in § 3. In § 4 we explore the nature of the 74 MHz radio source population. In § 5, we identify the ultra-steep spectrum sources and present high-resolution follow-up radio observations to determine their identities.

2. OBSERVATIONAL METHODOLOGY

2.1. *The Data Set*

The data used to produce this survey come from observations taken on 1998 March 7 intended to map two normal galaxies at 74 MHz (NGC 4565 and NGC 4631). Though these two targets were largely resolved out at this resolution, the combination of A configuration resolution, favorable ionospheric conditions, and pointings near the north Galactic pole, where the background temperature is low, produced the deepest observation ever obtained below 100 MHz. That the two fields observed were separated by 6°.4, which is roughly the radius of the primary beam at 74 MHz, allowed the two fields to be ideally combined to produce a single deep image of an area roughly $17° \times 10°$ in size.

The data were taken in spectral line mode to reduce bandwidth smearing and to facilitate removal of radio frequency interference. The total bandwidth of 1.54 MHz was divided into 128 channels, which Hanning smoothing reduced to 64. The central frequency was 73.8 MHz, and the integration time was 10 s. Each of the two pointings was observed for 3 hr, and the observation alternated between the two fields to better distribute the *uv* coverage.

2.2. *Challenges for High-Resolution Imaging at Low Frequency*

There are many challenges to high-resolution imaging at low radio frequencies that have prevented this observational regime from being explored until the past few years. In this

section, we summarize these issues and their solutions. N. E. Kassim et al. (2004) provide a more comprehensive description of 74 MHz observations with the VLA. In addition, a low-frequency data reduction tutorial is available online.[7]

2.2.1. *Radio Frequency Interference*

The monitor and control system of the VLA generates significant radio frequency interference (RFI) below 100 MHz, and there is the potential for external RFI as well. For this reason (and others) the data are acquired in spectral-line mode. Excision of potential RFI is performed on a per baseline basis for each visibility sample. Actual excision is accomplished by correcting the spectral-line data for the shape of the VLA bandpass at this frequency, fitting a linear baseline, then flagging any data exceeding a level typically set to be 6–8 times the expected rms noise level.[8] Typically, this procedure removes 10%–15% of the visibility data. It is notable, however, that at 74 MHz there is no evidence to indicate that any of this RFI is externally generated.

2.2.2. *The "Three-dimensional Problem"*

One crucial aspect for the postprocessing of these data sets is the need for a three-dimensional inversion of the visibility data. A conventional two-dimensional inversion of the three-dimensional visibility function, as measured by a noncoplanar (i.e., non–east-west) array like the VLA, introduces errors in the image plane that increase as the square of the distance from the phase center. The "three-dimensional" problem becomes severe at long wavelengths where the primary beam is large and contains hundreds of discrete sources that must be properly deconvolved to achieve thermal-noise– or classical-confusion–limited maps.

To solve this problem, Cornwell & Perley (1992) have developed a polyhedron algorithm in which the three-dimensional "image volume" is approximated by many two dimensional "facets," small enough that the traditional two-dimensional assumption is valid. Thus, a "fly's eye" of small overlapping images, each with its own phase center, is made to cover the large field of view. Typically, many hundreds of facets are needed to map the full primary beam area, and after cleaning and imaging, these images are then combined into a single undistorted image of the full field of view.

2.2.3. *Ionospheric Image Distortion*

The biggest challenge to achieving high resolution at low frequencies is the distortion of phases caused by the ionosphere, an effect that increases proportionally with wavelength (Kassim et al. 1993). This problem is compounded by the fact that the field of view at 74 MHz is so large that these phase distortions can vary significantly across the field of view. This puts phase calibration of 74 MHz data into an entirely different regime from higher frequencies in which all phase distortions can be completely described by a single time-variable number for each antenna. For this reason, traditional self-calibration does not apply. Rather, a field-based calibration method, in which the phase calibration is position-dependent, is needed. Such an algorithm has been written by J. J. Condon and W. D. Cotton[9] (Cotton & Condon 2002). This algorithm models the ionosphere as a phase screen varying in space and

---

[5] See http://www.lofar.org.
[6] See http://www.skatelescope.org.

[7] See http://rsd-www.nrl.navy.mil/7213/lazio/tutorial.
[8] This algorithm is contained within the AIPS task FLGIT.
[9] VLAFM: a special-purpose task designed to work within AIPS.

time, and it applies a two-dimensional Zernike polynomial phase correction to correct the phases across the entire field of view.

2.3. *Data Reduction*

Cygnus A (3C 405) was used for bandpass and amplitude calibration. Phase calibration was more complicated. As described in § 2.2.3, calibration that applies a constant phase correction to the entire field is insufficient for imaging of the entire 74 MHz VLA primary beam, and field-based calibration is needed. However, an initial calibration estimate is necessary to begin the field-based calibration, and so as a first step, we calibrated the field to a sky model obtained using the 1.4 GHz NVSS catalog (Condon et al. 1998) adjusted for a spectral index of $\alpha = -0.75$.[10] Next, field-based calibration was used to remove ionospheric smearing before imaging and cleaning were performed.[11] The field-based calibration was performed with a time resolution of 2 minutes, enough to significantly detect an average of 6 to 10 sources in the field of view. Each pointing was mapped to a radius of $6°$ using roughly 300 facets. We used a pixel size of $7\overset{''}{.}5$, and each facet was 360 pixels in diameter. A circular $25''$ restoring beam was used. The images from the two fields were then corrected for the primary beam shape and co-added to produce a single image.

3. RESULTS

3.1. *Image Quality*

Our final image has a resolution of $25''$ and a minimum rms noise level of 24 mJy beam^{-1}, a unique combination for such a low-frequency survey (see Fig. 1). However, the noise level varies over the image due to the primary beam sensitivity patterns for the two fields, the added sensitivity due to the two fields overlapping and occasional incompletely cleaned sidelobes from bright sources (Fig. 2). The image has no real "edge," just an increase in the noise level with distance from the pointing centers. If we define the survey area as the area in our map for which the rms noise is lower than a set limit, then as this limit is increased the survey area increases. However, at points more than about $5°$ from either pointing center the noise level begins to increase so rapidly that the benefits of increasing the survey area quickly diminish (see Table 1). We chose the field edge to be at the 80 mJy beam^{-1} noise level, which defines a total survey area of 165.1 deg^2, with almost half of this area having a sensitivity below 40 mJy beam^{-1}.

3.2. *Source Extraction*

The same algorithm that was written for use in the 1.4 GHz NVSS (Condon et al. 1998) was used to identify and characterize sources in this 74 MHz survey.[12] This algorithm works by identifying "islands" of emission in the image above a set threshold and fitting each source to a model of up to four Gaussians. We set as our source detection threshold that sources must have both a peak and integrated flux level at least 5 times the local rms noise level. Therefore, the source detection threshold varies over the image as the rms noise varies.

We combined into multiple sources (sources composed of more than one Gaussian component), those sources located within $120''$ of each other. This distance was chosen because it corresponds to the separation distance of radio sources for
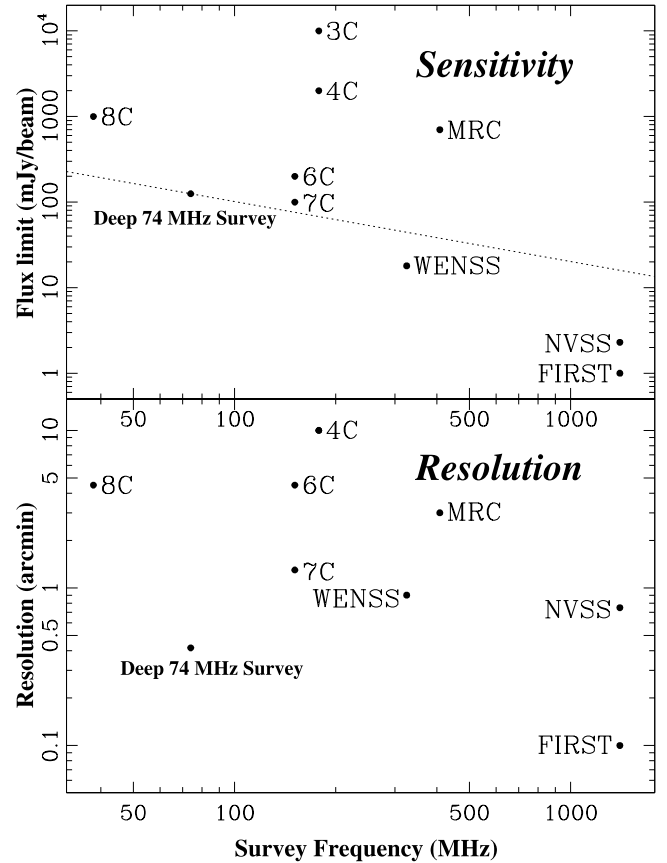
Fig. 1.—Sensitivity (5 σ) and resolution of our deep 74 MHz radio survey compared to that of the major low-frequency radio surveys. The dotted line on the sensitivity plot (*top*) shows the flux density of a source at our sensitivity limit assuming a spectral index of $\alpha = -0.7$.

which doubles that are components of the same source (usually a radio galaxy) outnumber those that are actually two separate objects by a ratio of 10 to 1 as determined by a recent study of the clustering of radio sources in the NVSS (Overzier et al. 2003). In total, we detected 949 sources (Fig. 3) with integrated fluxes ranging from 146 mJy to 39.9 Jy. Of these, 70 were multiple sources. Most sources were not much larger than the $25''$ beam size, with only 75 sources (7.9%) measuring larger than two beam widths across, either as the fitted size of a single source or the maximum separation within a multiple source. Most of the extended sources appear to be FR II type radio galaxies. Figure 4 shows contour maps of the 80 largest sources in the survey. A complete catalog of all sources is available in the electronic edition in Table 2.

4. SOURCE STATISTICS

4.1. *Source Counts*

We present Euclidean-normalized differential source counts in Figure 5. These were calculated within flux density bins of size $\pm 15\%$ from the central flux density. To ensure a true measure of source densities, for each flux density bin we only considered the region of the survey in which all sources in that flux density bin are detected with at least 7 σ confidence, the canonical level of 2 σ completeness for sources selected above a 5 σ threshold. Thus, for each flux density bin we only selected sources from the region of the survey with a noise level lower than 1/7 of the lower flux density limit of that bin.
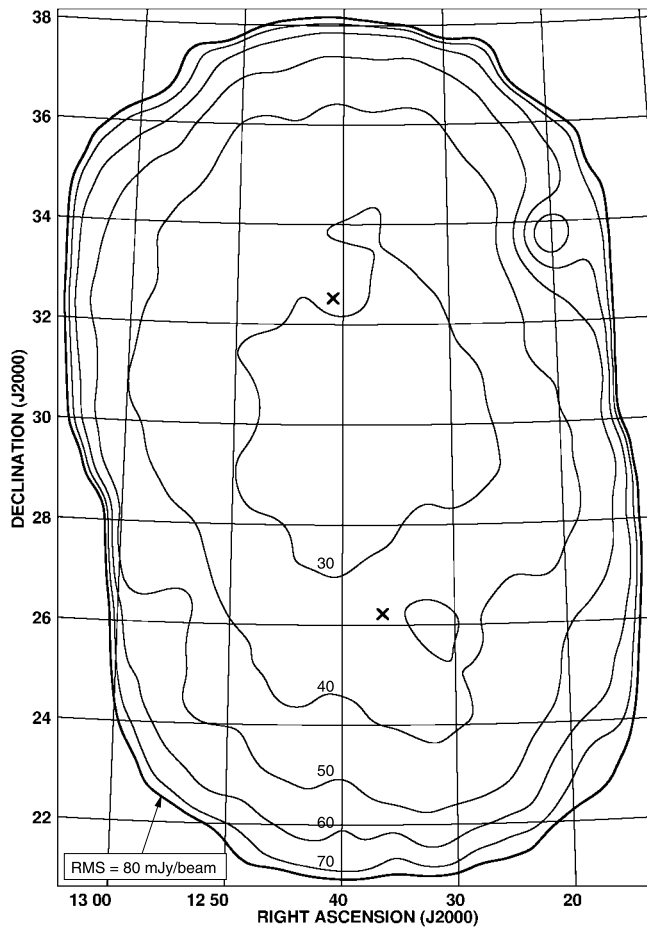
FIG. 2.—Noise levels in the 74 MHz survey area as determined by local measurements of the rms noise in the image. The contours plotted are at 30, 40, 50, 60, 70, and 80 mJy beam^{-1}, with the outermost contour at 80 mJy beam^{-1} in bold defining the boundary of the survey. Each of the two field centers is marked with a cross.

The source density was calculated by dividing this source count by the area of that "7 σ" region from which the sources were selected.

Also plotted in Figure 5 is a polynomial fit to the source count at 327 MHz (Wieringa 1991) and its adjustments according to various spectral indices. The data at 74 MHz seem to correspond to an average spectral index of somewhere between $\alpha = -0.5$ and $\alpha = -0.75$, though there seems to be an overall trend of steeper corresponding spectral index at higher flux levels. We caution that this is not a direct measurement of

the average spectral index as many compact sources seen at 327 MHz are not seen at 74 MHz due to synchrotron self-absorption.

We note that the differential source counts function depends to some degree on our choice of spatial cutoff for grouping sources. Though we grouped components closer than 120″ into single sources, if larger physical sources were broken into multiple "sources," the differential source counts function would be artificially increased for lower flux densities and decreased for the highest flux densities. However, this effect is likely to be minor. For example, if we double the spatial cutoff to 240″, only 35 additional sources (3.7%) are "grouped." Further, it is unlikely that all of these new multiple sources are physical, with (Overzier et al. 2003) predicting near parity between physical and coincidental doubles at a spacing of 240″.

4.2. *Comparisons to Other Survey Catalogs*

We compared our source catalog to the 1.4 GHz NVSS catalog (Condon et al. 1998), which, with its resolution of 45″, is well enough matched to our resolution to provide accurate spectral index measurements. The long frequency interval between 74 MHz and 1.4 GHz also contributes to the accuracy of the spectral index measurements as a flux ratio error of 10% produces a spectral index error of only $\Delta\alpha = 0.032$. We found NVSS matches within 60″ for 947 out of our total of 949 sources. The two sources without NVSS matches were J1230.6+3247 and J1253.6+2509, implying very steep spectral index upper limits of -1.47 and -1.78, respectively. It is therefore reasonable to wonder if these are real detections. The peak flux density of J1230.6+3247 was measured to be 188 mJy beam^{-1}, which is a 6.3 σ detection given the local noise level of 29.8 mJy beam^{-1}. This relatively strong detection and the fact that the spectral index necessary to explain the lack of detection is, though very steep, not even the steepest in the survey, led us to conclude that this source is probably real. The peak flux density of J1253.6+2509 was measured to be 256 mJy beam^{-1}, which was just barely over our 5 σ detection threshold for the local noise level of 50.4 mJy beam^{-1}. Because of this and the extraordinary steepness of its spectrum necessary to explain its lack of detection by NVSS, we conclude that it is a non-negligible possibility that this may be a false detection. However, as it meets our criteria for a source detection, we still include it in our source list.

We present the spectral index measurements in Figure 6 plotted versus the integrated flux density at 74 MHz. The spectral indices of all sources with respect to their NVSS counterparts are included in the source catalog. We find a

TABLE 1
SURVEY AREA

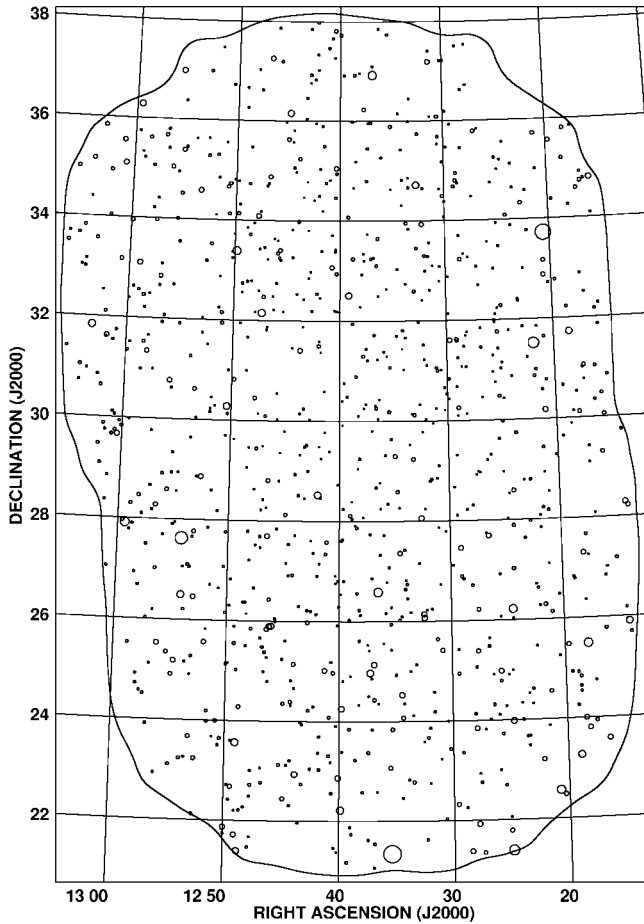| Noise Limit (mJy beam^{-1})	Area (deg^2)	Source Count (number)
25..	2.5	23
27..	8.6	62
30..	22.4	158
35..	50.0	356
40..	78.2	535
50..	119.1	765
60..	142.7	873
70..	156.9	924
80..	165.1	949

Fig. 3.—Location of all sources identified at the 5 σ level within the survey region. The area of each circle is proportional to the integrated flux of that source. The weakest source is 146 mJy and the strongest is 39.9 Jy.

median spectral index of $\alpha = -0.79$. Figure 7 shows the spectral index as a function of 74 MHz flux density, and it is clear that the average spectral index steepens with increasing flux density.

In addition to the spectral index between the widely spaced frequencies of 74 MHz and 1.4 GHz, it is of interest to investigate the actual shape of the spectrum within this interval. For this, we turn to the 327 MHz WENSS survey (Rengelink et al. 1997). Although the WENSS only covers the northern sky down to a declination of $+29°$, which falls near the middle of our survey region, we find counterparts (within $60''$) to 545 sources. Figure 8 shows a comparison of the spectral indices for two frequency intervals in the form of a radio color-color plot. As this plot shows, most source spectra flatten considerably from the "low" frequency interval from 327 MHz to 1.4 GHz to the "very low" frequency interval from 74 to 327 MHz. Quantitatively, we found a median change in the spectral index of $\Delta\alpha = 0.24$.

We also compared our source catalog to the higher resolution ($5''.4$) 1.4 GHz FIRST survey (White et al. 1997). We found matches within $30''$ for 945 out of our total of 949 sources (including neither of the two sources without NVSS matches). This allowed a much better measurement of source sizes than was possible with the $25''$ resolution of the 74 MHz observations. We define the source size as either the deconvolved major axis for single sources in FIRST or as the maximum separation between components for the multiple sources.

Overall, we find a median source size of $8''.1$, though we notice a strong correlation between source size and spectral index. Figure 9 shows the median source size as a function of spectral index along with a spectral index histogram. It is clear that the steeper the spectrum the larger the sources, which makes sense as one would expect compact sources to have flatter spectra on average due to synchrotron self-absorption, although this trend seems to stall if not reverse for the very steep spectrum objects ($\alpha < -1$).

5. ULTRA-STEEP SPECTRUM SOURCES
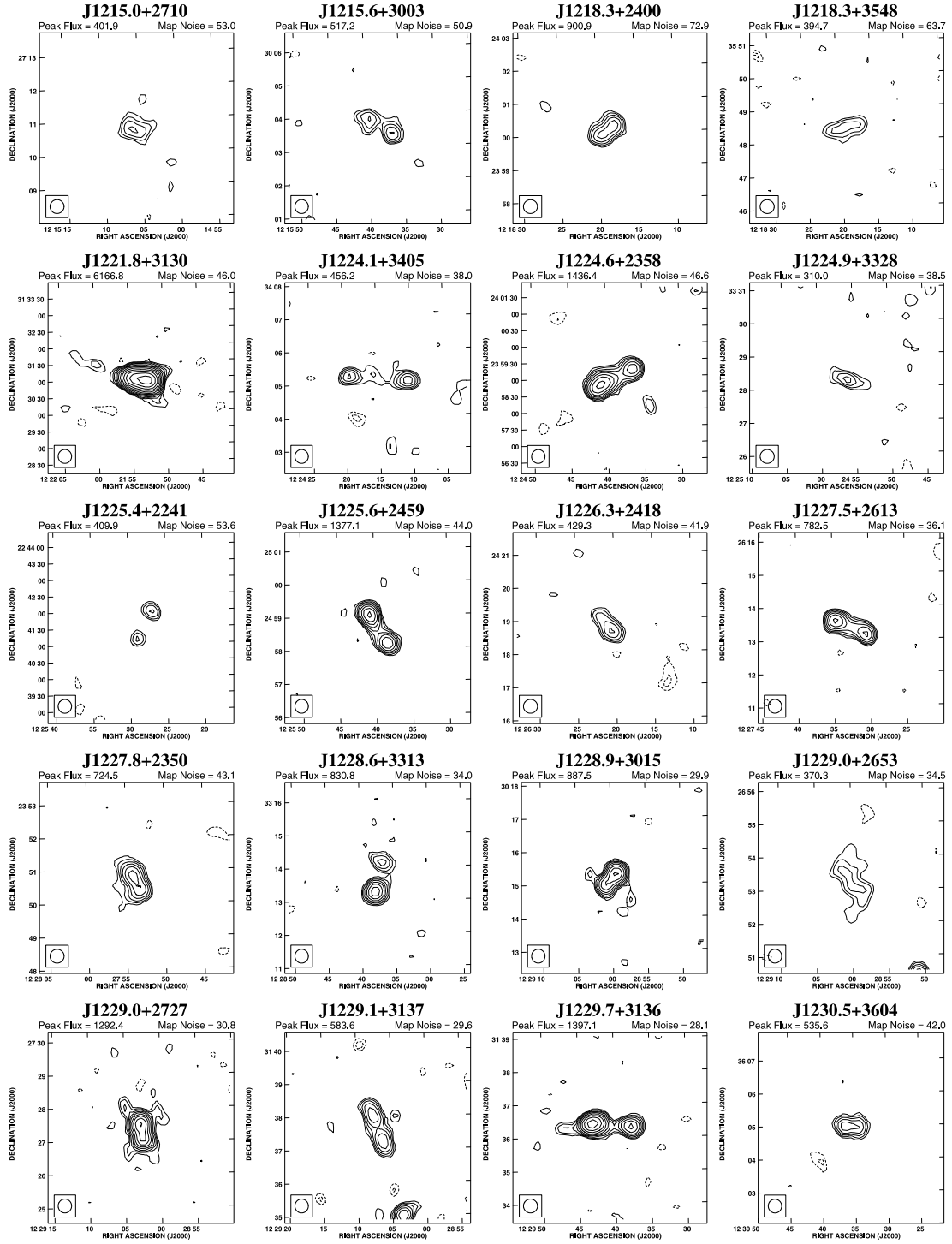
5.1. Identification and Follow-up

To identify our sample of ultra-steep spectrum (USS) sources, we chose a spectral index cutoff of $\alpha_{74}^{325} < -1.2$. With this criterion, we identified 26 USS sources out of a total of 949 sources (2.7%). This included 24 sources with measured spectral indices and the two sources with no FIRST or NVSS counterparts, which have spectral index upper limits that qualify them as USS as well.

This percentage of USS sources is much higher than that found in the previous USS searches by De Breuck et al. (2000), which found a USS fraction of only 0.5%. Even if we use their stricter USS criteria of $\alpha < -1.3$, we still have detected 18 USS sources, or 1.9%. It is unclear exactly what causes this difference, but it is possibly due to a combination of effects. First, by selecting sources at 74 MHz, rather than 325, we have eliminated virtually the entire population of flat spectrum objects from our sample. Second, as 74 MHz observations are less sensitive than those at higher frequencies, we have a brighter sample, and it is known that as the flux limit increases, the USS fraction increases.

There are four main possibilities for the identities of such USS sources: (1) pulsars, (2) high-redshift radio galaxies (HzRGs: $z > 2$), (3) cluster halos or relics (CHRs) and (4) fossil radio galaxies (FRGs: radio galaxies for which the energized particles have undergone significant spectral aging). As this survey is located near the north Galactic pole, we expect very few if any pulsars. Using the most recent estimate for the radio luminosity function of CHRs (Enßlin & Röttgering 2002), we predict that on the order of one CHR will be detectable in this region given our sensitivity limit, so this is a real possibility. HzRGs, cluster halos, and FRGs can be distinguished by their morphologies. We expect small ($\leq 30''$) FR II morphologies for HzRGs, while cluster halos or FRGs will be much larger and more diffuse. It is difficult to qualify the morphology with the $25''$ resolution of our 74 MHz images, so again we turn to the 1.4 GHz FIRST survey (White et al. 1997) with its resolution of $5''.4$. In Figure 10 we present FIRST images of each of the 24 USS sources with an NVSS counterpart. Comparison with the POSS II shows matches or possible matches to four of 24 sources, roughly consistent with the 15% reported by De Breuck et al. (2000). We have also begun our own follow-up observations at 1.4 GHz with the VLA in A configuration, which provides roughly $1''.4$ resolution. So far we have so observed 18 of the 24 USS sources with NVSS counterparts, and 11 of these were detected (Fig. 11), with the remaining seven likely resolved out. A list of all USS sources we found is provided in Table 2, and brief descriptions of each USS source follows below.

5.2. Brief Description of Individual USS Sources

The following are brief notes on each USS source. Source images at 1.4 GHz are described from FIRST ($5''.4$ resolution)

J1215.0+2710
Peak Flux = 401.9   Map Noise = 53.0

J1215.6+3003
Peak Flux = 517.2   Map Noise = 50.9

J1218.3+2400
Peak Flux = 900.9   Map Noise = 72.9

J1218.3+3548
Peak Flux = 394.7   Map Noise = 63.7

J1221.8+3130
Peak Flux = 6166.8   Map Noise = 46.0

J1224.1+3405
Peak Flux = 456.2   Map Noise = 38.0

J1224.6+2358
Peak Flux = 1436.4   Map Noise = 46.6

J1224.9+3328
Peak Flux = 310.0   Map Noise = 38.5

J1225.4+2241
Peak Flux = 409.9   Map Noise = 53.6

J1225.6+2459
Peak Flux = 1377.1   Map Noise = 44.0

J1226.3+2418
Peak Flux = 429.3   Map Noise = 41.9

J1227.5+2613
Peak Flux = 782.5   Map Noise = 36.1

J1227.8+2350
Peak Flux = 724.5   Map Noise = 43.1

J1228.6+3313
Peak Flux = 830.8   Map Noise = 34.0

J1228.9+3015
Peak Flux = 887.5   Map Noise = 29.9

J1229.0+2653
Peak Flux = 370.3   Map Noise = 34.5

J1229.0+2727
Peak Flux = 1292.4   Map Noise = 30.8

J1229.1+3137
Peak Flux = 583.6   Map Noise = 29.6

J1229.7+3136
Peak Flux = 1397.1   Map Noise = 28.1

J1230.5+3604
Peak Flux = 535.6   Map Noise = 42.0

Note: Peak flux and map noise values are given in mJy/beam. Contours begin at 2.5 times the map noise and increase by factors of sqrt(2).

FIG. 4.—Maps of the 80 largest objects detected at 74 MHz. These objects all have a fitted source size (for single sources) or maximum separation between components (for multiple sources) of at least 48″.4.

J1231.3+3711
Peak Flux = 279.8 Map Noise = 51.2

J1231.5+2849
Peak Flux = 359.0 Map Noise = 29.5

J1231.6+3317
Peak Flux = 228.4 Map Noise = 33.2

J1232.0+3001
Peak Flux = 165.0 Map Noise = 22.1

J1232.1+2340
Peak Flux = 481.8 Map Noise = 40.2

J1233.0+3007
Peak Flux = 538.8 Map Noise = 25.9

J1233.9+2644
Peak Flux = 208.1 Map Noise = 34.0

J1234.3+2404
Peak Flux = 1247.1 Map Noise = 40.9

J1234.5+2721
Peak Flux = 917.5 Map Noise = 30.2

J1235.3+2120
Peak Flux = 6712.4 Map Noise = 79.9

J1235.3+2556
Peak Flux = 474.0 Map Noise = 38.2

J1235.5+2704
Peak Flux = 239.0 Map Noise = 33.5

J1236.8+2508
Peak Flux = 1207.4 Map Noise = 36.2

J1237.4+3447
Peak Flux = 301.4 Map Noise = 33.0

J1238.4+2633
Peak Flux = 287.9 Map Noise = 34.4

J1238.4+2752
Peak Flux = 277.8 Map Noise = 30.4

J1238.4+3053
Peak Flux = 298.9 Map Noise = 25.8

J1239.8+2736
Peak Flux = 311.7 Map Noise = 28.6

J1239.8+2213
Peak Flux = 3854.9 Map Noise = 57.1
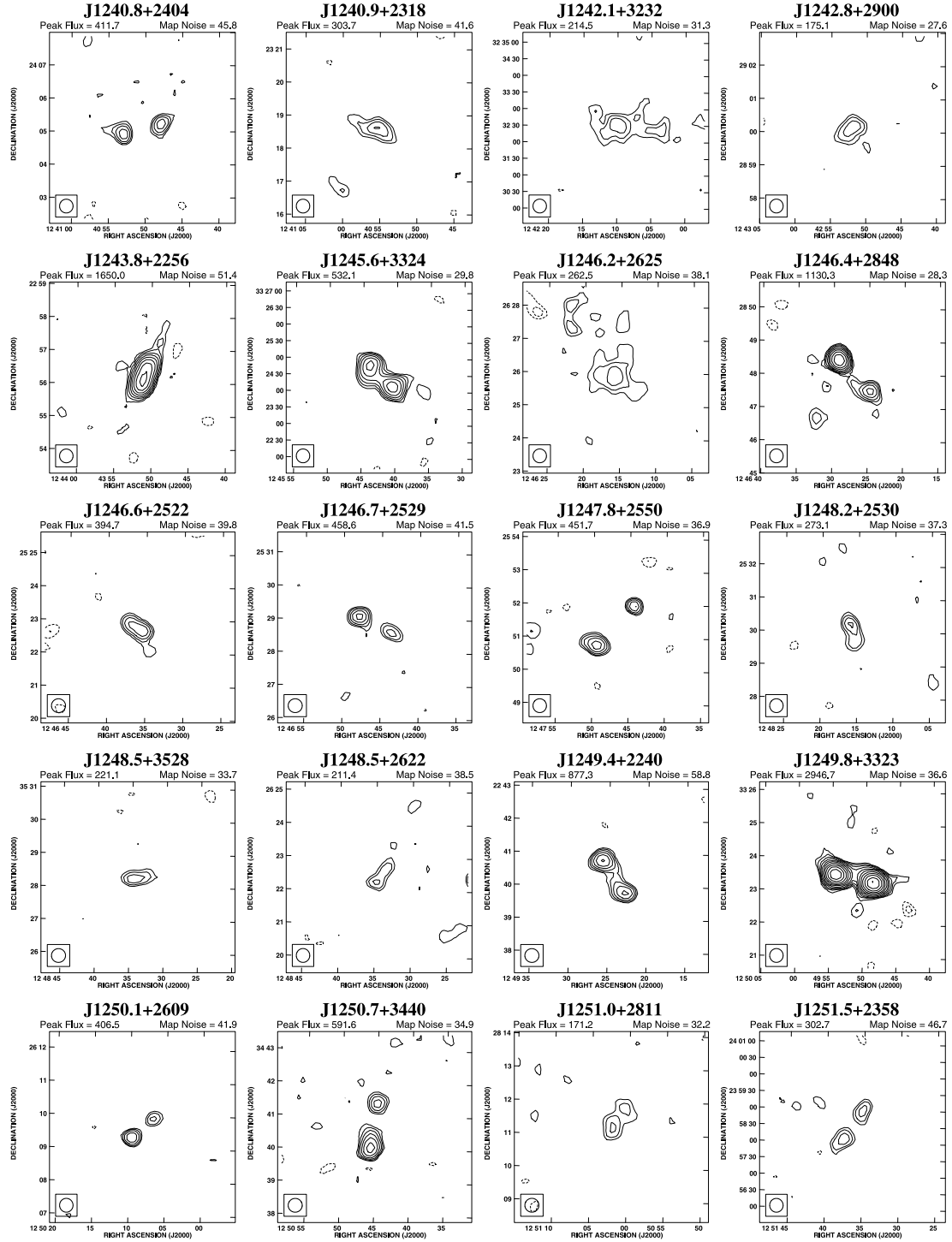
J1239.9+3743
Peak Flux = 427.4 Map Noise = 52.0

Note: Peak flux and map noise values are given in mJy/beam. Contours begin at 2.5 times the map noise and increase by factors of sqrt(2).

Fig. 4.—*Continued*

423

J1240.8+2404 Peak Flux = 411.7 Map Noise = 45.8
J1240.9+2318 Peak Flux = 303.7 Map Noise = 41.6
J1242.1+3232 Peak Flux = 214.5 Map Noise = 31.3
J1242.8+2900 Peak Flux = 175.1 Map Noise = 27.6

J1243.8+2256 Peak Flux = 1650.0 Map Noise = 51.4
J1245.6+3324 Peak Flux = 532.1 Map Noise = 29.8
J1246.2+2625 Peak Flux = 262.5 Map Noise = 38.1
J1246.4+2848 Peak Flux = 1130.3 Map Noise = 28.3

J1246.6+2522 Peak Flux = 394.7 Map Noise = 39.8
J1246.7+2529 Peak Flux = 458.6 Map Noise = 41.5
J1247.8+2550 Peak Flux = 451.7 Map Noise = 36.9
J1248.2+2530 Peak Flux = 273.1 Map Noise = 37.3

J1248.5+3528 Peak Flux = 221.1 Map Noise = 33.7
J1248.5+2622 Peak Flux = 211.4 Map Noise = 38.5
J1249.4+2240 Peak Flux = 877.3 Map Noise = 58.8
J1249.8+3323 Peak Flux = 2946.7 Map Noise = 36.6

J1250.1+2609 Peak Flux = 406.5 Map Noise = 41.9
J1250.7+3440 Peak Flux = 591.6 Map Noise = 34.9
J1251.0+2811 Peak Flux = 171.2 Map Noise = 32.2
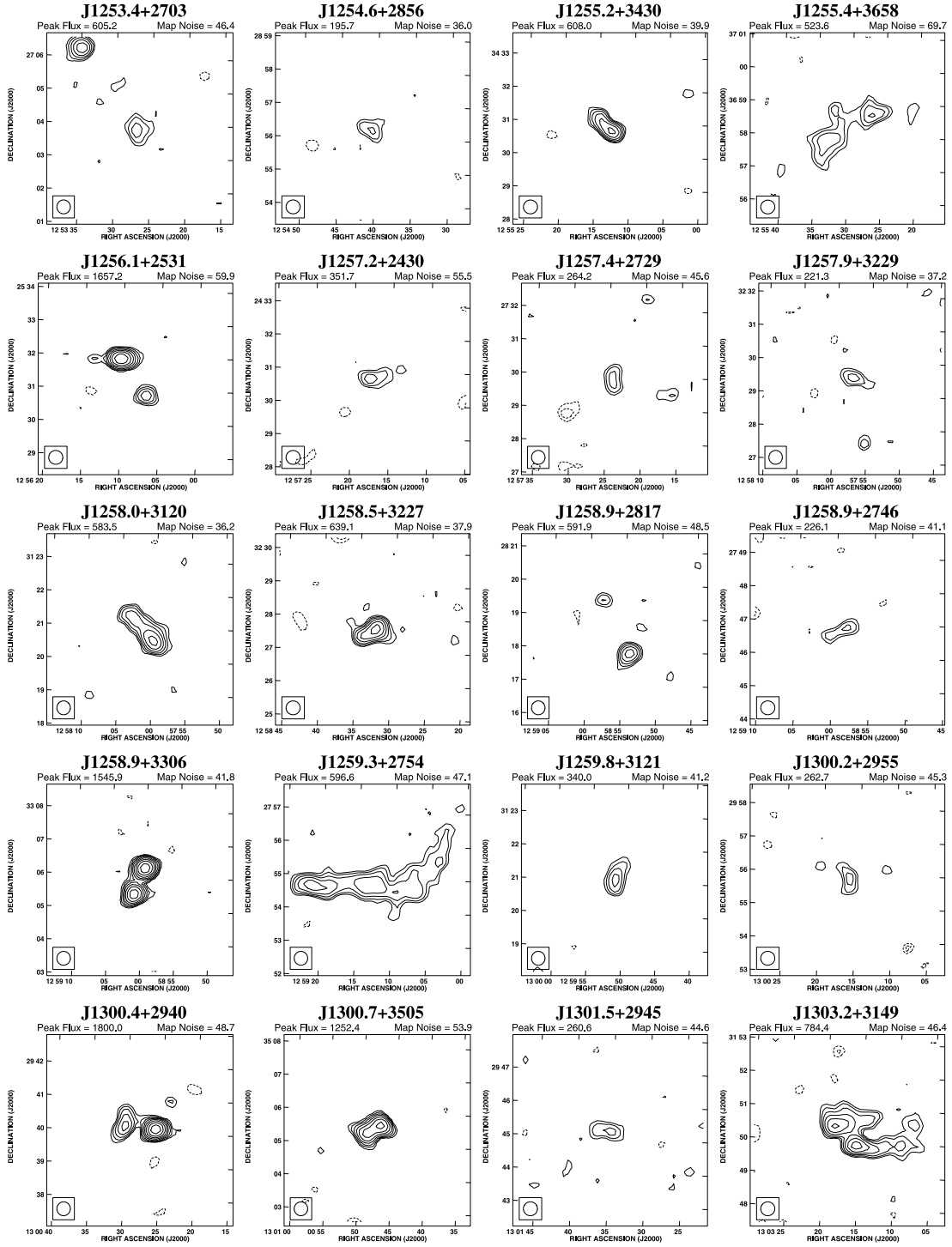J1251.5+2358 Peak Flux = 302.7 Map Noise = 46.7

Note: Peak flux and map noise values are given in mJy/beam. Contours begin at 2.5 times the map noise and increase by factors of sqrt(2).

Fig. 4.—*Continued*

424

J1253.4+2703
Peak Flux = 605.2   Map Noise = 46.4

J1254.6+2856
Peak Flux = 195.7   Map Noise = 36.0

J1255.2+3430
Peak Flux = 608.0   Map Noise = 39.9

J1255.4+3658
Peak Flux = 523.6   Map Noise = 69.7

J1256.1+2531
Peak Flux = 1657.2   Map Noise = 59.9

J1257.2+2430
Peak Flux = 351.7   Map Noise = 55.5

J1257.4+2729
Peak Flux = 264.2   Map Noise = 45.6

J1257.9+3229
Peak Flux = 221.3   Map Noise = 37.2

J1258.0+3120
Peak Flux = 583.5   Map Noise = 36.2

J1258.5+3227
Peak Flux = 639.1   Map Noise = 37.9

J1258.9+2817
Peak Flux = 591.9   Map Noise = 48.5

J1258.9+2746
Peak Flux = 226.1   Map Noise = 41.1

J1258.9+3306
Peak Flux = 1545.9   Map Noise = 41.8

J1259.3+2754
Peak Flux = 596.6   Map Noise = 47.1

J1259.8+3121
Peak Flux = 340.0   Map Noise = 41.2

J1300.2+2955
Peak Flux = 262.7   Map Noise = 45.3

J1300.4+2940
Peak Flux = 1800.0   Map Noise = 48.7

J1300.7+3505
Peak Flux = 1252.4   Map Noise = 53.9

J1301.5+2945
Peak Flux = 260.6   Map Noise = 44.6

J1303.2+3149
Peak Flux = 784.4   Map Noise = 46.4

Note: Peak flux and map noise values are given in mJy/beam. Contours begin at 2.5 times the map noise and increase by factors of sqrt(2).

Fig. 4.—*Continued*

TABLE 2
USS SOURCE LIST

Source	α (J2000)	δ (J2000)	$S_{74,\,int}$ (Jy)	α_{74}^{1400}	POSS II ID
J1225.0+2146........................	12 25 02.26	+21 46 52.5	2.213	−1.25	N
J1226.3+2418........................	12 26 20.65	+24 18 43.6	0.943	−1.36	Y
J1228.9+3114........................	12 28 59.58	+31 14 57.6	0.608	−1.36	N
J1229.1+3040........................	12 29 07.75	+30 40 41.2	0.356	−1.27	N
J1229.9+3712........................	12 29 58.03	+37 12 48.8	0.635	−1.25	N
J1230.2+2326........................	12 30 14.05	+23 26 17.2	0.968	−1.63	Y
J1230.6+3247........................	12 30 37.90	+32 47 21.9	0.188	< −1.47	
J1231.2+2538........................	12 31 15.08	+25 38 26.3	1.064	−1.20	?
J1231.3+3724........................	12 31 20.77	+37 24 17.4	0.477	−1.51	N
J1231.5+3236........................	12 31 32.71	+32 36 30.1	0.311	−1.52	N
J1232.2+2814........................	12 32 13.76	+28 14 34.9	0.327	−1.36	N
J1232.6+3157........................	12 32 38.23	+31 57 52.1	0.359	−1.35	N
J1234.3+2605........................	12 34 23.25	+26 05 50.5	0.402	−1.61	N
J1238.2+2613........................	12 38 12.40	+26 13 45.8	0.728	−1.30	N
J1238.8+3559........................	12 38 49.30	+35 59 22.9	0.634	−1.33	N
J1243.7+2830........................	12 43 42.75	+28 30 55.5	0.712	−1.73	N
J1245.9+3320........................	12 45 54.20	+33 20 32.1	1.140	−1.40	N
J1246.4+2516........................	12 46 24.49	+25 16 35.1	0.347	−1.29	N
J1248.2+2747........................	12 48 13.51	+27 47 22.6	0.624	−1.31	N
J1249.0+3615........................	12 49 01.82	+36 15 46.8	0.440	−1.20	?
J1249.7+3408........................	12 49 43.34	+34 08 09.2	1.383	−1.23	N
J1250.4+2941........................	12 50 28.33	+29 41 43.8	0.395	−1.35	N
J1252.7+2207........................	12 52 44.13	+22 07 04.9	0.940	−1.22	N
J1253.4+2703........................	12 53 26.85	+27 03 50.0	0.838	−1.30	N
J1253.6+2509........................	12 53 39.24	+25 09 57.7	0.472	< −1.78	
J1256.9+2811........................	12 56 58.15	+28 11 09.7	0.524	−1.32	N

NOTES.—Units of right ascension are hours, minutes, and seconds, and units of declination are degrees, arcminutes, and arcseconds. Table 2 is available in its entirety in the electronic edition of the *Astrophysical Journal Supplement*. A portion is shown here for guidance regarding its form and content. The print version of the table includes all 26 ultra-steep spectrum sources. The electronic version includes all 949 sources in the survey.
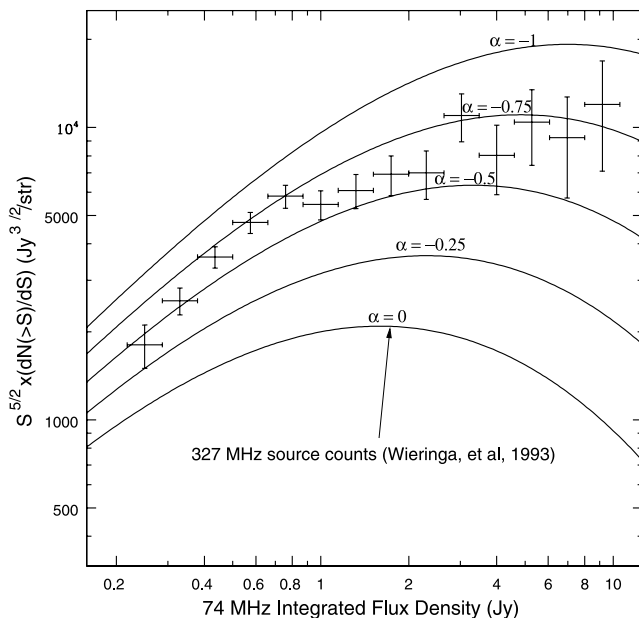

FIG. 5.—Euclidean-normalized differential source count. Also plotted are source counts at 327 MHz (Wieringa 1991) adjusted for various spectral indices.

and or VLA A configuration follow-up (1″4 resolution). We speculate on the identity of each source from the four main classes of USS objects: pulsar, cluster halo/relic (CHR), fossil radio galaxy (FRG), or high-redshift radio galaxy (HzRG).

J1225.0+2146.—The FIRST map shows a bright double lobed FR II with a separation of roughly 25″. This is likely to be a HzRG or FRG.

J1226.3+2418.—The FIRST map shows a 20″ FR II with diffuse extension. A configuration resolved out this source. It was identified in the POSS II so it probably is not high redshift. This is likely to be a FRG.

J1228.9+3114.—The FIRST map shows a diffuse blob of about 15″, which is resolved out in A configuration. This is likely to be a high-*z* CHR, HzRG, or FRG.

J1229.1+3040.—Unresolved in FIRST but a fit to the A configuration map shows a source size of about 1″. This is likely a HzRG.

J1229.9+3712.—Head-tail morphology in FIRST map. This is likely to be a HzRG or FRG.

J1230.2+2326.—Faint double source in FIRST maps, resolved out in A configuration. It was identified in the POSS II so it probably is not high redshift. This is likely to be a FRG.

J1230.6+3247.—No FIRST or NVSS counterpart.

J1231.2+2538.—A configuration shows core-jet morphology with an extent of 12″. This is likely to be a HzRG or FRG.

J1231.3+3724.—Unresolved in FIRST. This is likely to be a pulsar or HzRG.

J1231.5+3236.—Resolved out in FIRST and A configuration. This is likely to be a high-*z* CHR or FRG.
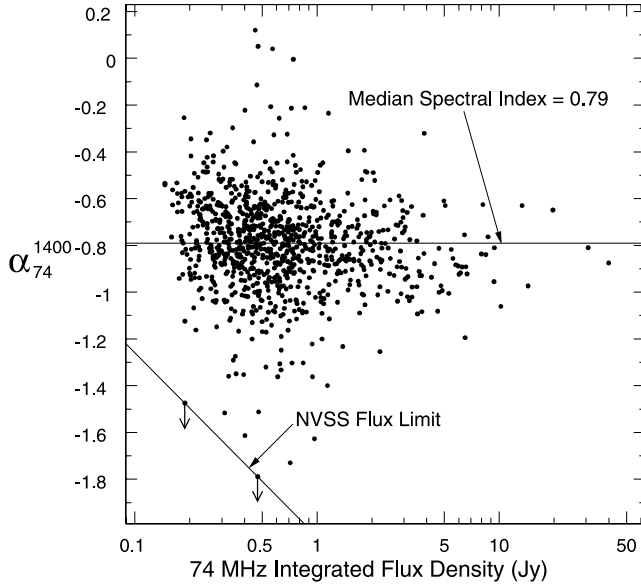
Fig. 6.—Spectral indices (α_{74}^{1400}) vs. 74 MHz integrated flux density. Spectral index upper limits are plotted for the two sources without NVSS detections.

J1232.2+2814.—Unresolved in FIRST and A configuration maps. This is likely to be a pulsar or HzRG.

J1232.6+3157.—A configuration shows a 7″ FR II with much diffuse emission. This is likely to be a high-*z* CHR, HzRG, or FRG.

J1234.3+2605.—Unresolved in FIRST but a fit to the A configuration map shows a source size of about 1″. This is likely a HzRG.

J1238.2+2613.—Unresolved in FIRST but a fit to the A configuration map shows a source size of about 0.″5. This is likely a HzRG.

J1238.8+3559.—FIRST and A configuration show a well defined 17″ FR II. This is likely to be a HzRG or FRG.

J1243.7+2830.—FIRST and A configuration show a faint 2″ elongated object. This is likely to be a HzRG or FRG.

Fig. 8.—Radio color-color diagram of the 545 of 949 sources with both an NVSS and a WENSS counterpart. The diagonal line represents the location of sources for which $\alpha_{74}^{325} = \alpha_{325}^{1400}$. For most sources, the spectrum flattens considerably in the lower frequency interval.

J1245.9+3320.—FIRST shows a roughly 15″ FR I morphology, which is resolved out in A configuration. This is likely to be a high-*z* CHR or FRG.

J1246.4+2516.—FIRST shows a roughly 10″ blob, which is resolved out in A configuration. This is likely to be a high-*z* CHR or FRG.

J1248.2+2747.—FIRST and A configuration show a faint 6″ FR II morphology. This is likely to be a HzRG or FRG.

Fig. 7.—Mean spectral index vs. 74 MHz flux density. The horizontal error bars correspond to the bin widths.
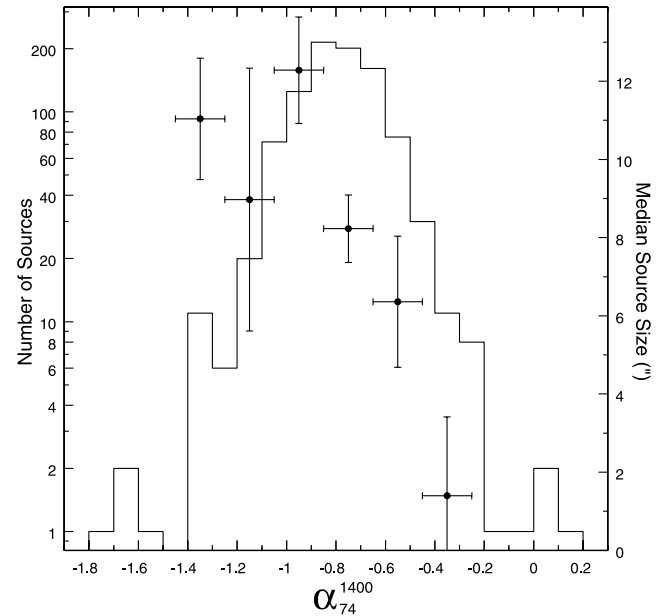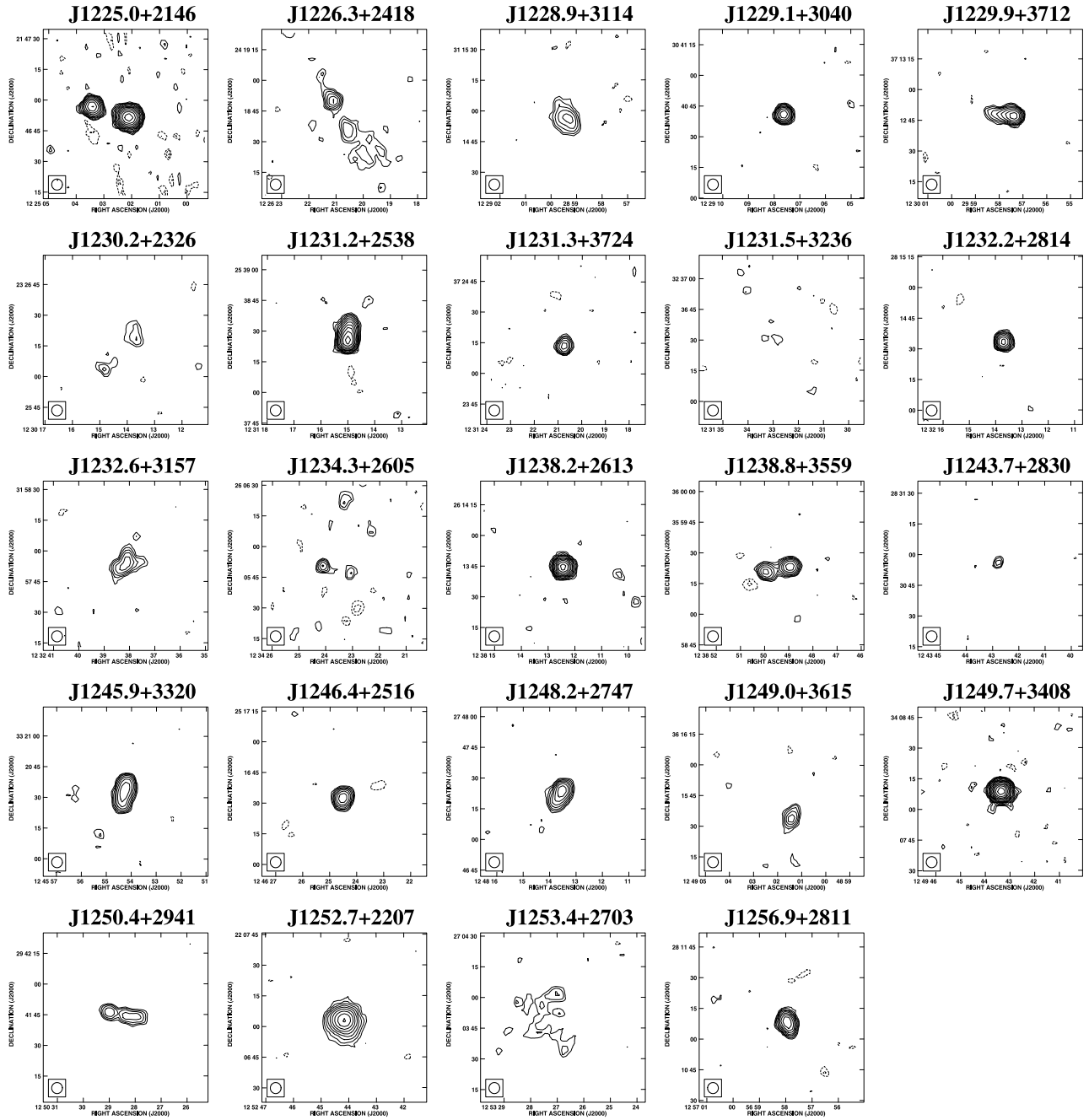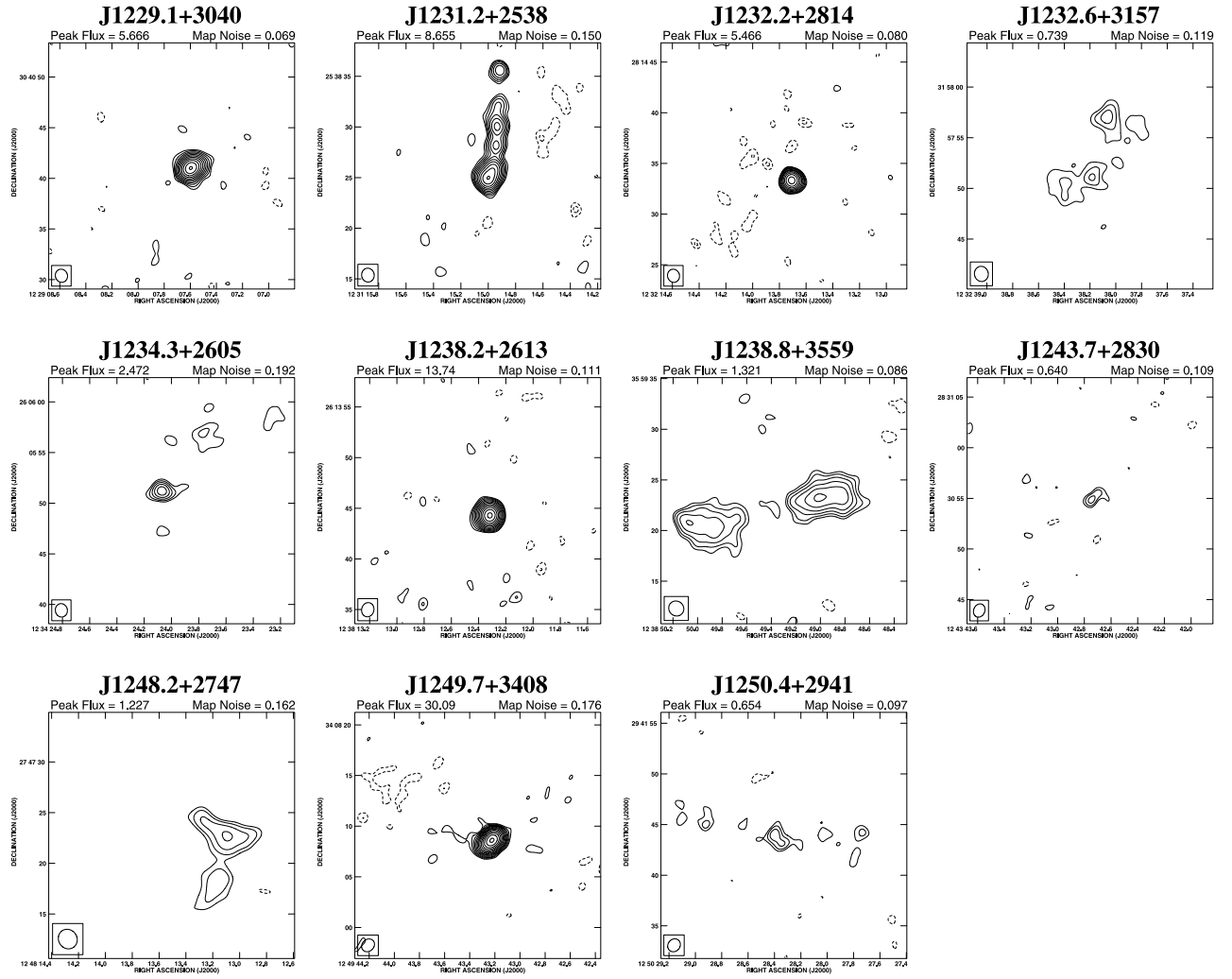

Fig. 9.—Spectral histogram along with median sources sizes as a function of spectral index. Source sizes are determined with the FIRST images, while spectral indices are determined using the 74 MHz integrated flux density and the NVSS flux densities. Not enough sources were detected with $\alpha_{74}^{1400} < -1.45$ or $\alpha_{74}^{1400} > -0.25$ for meaningful statistics in those regions.

J1225.0+2146 J1226.3+2418 J1228.9+3114 J1229.1+3040 J1229.9+3712

J1230.2+2326 J1231.2+2538 J1231.3+3724 J1231.5+3236 J1232.2+2814

J1232.6+3157 J1234.3+2605 J1238.2+2613 J1238.8+3559 J1243.7+2830

J1245.9+3320 J1246.4+2516 J1248.2+2747 J1249.0+3615 J1249.7+3408

J1250.4+2941 J1252.7+2207 J1253.4+2703 J1256.9+2811

Note: Contours begin at 0.4 mJy/beam and increase by factors of sqrt(2).

FIG. 10.—Images from the FIRST survey of the 24 of 26 ultra-steep spectrum sources identified at 74 MHz, which had NVSS counterparts

J1229.1+3040

Peak Flux = 5.666   Map Noise = 0.069

J1231.2+2538

Peak Flux = 8.655   Map Noise = 0.150

J1232.2+2814

Peak Flux = 5.466   Map Noise = 0.080

J1232.6+3157

Peak Flux = 0.739   Map Noise = 0.119

J1234.3+2605

Peak Flux = 2.472   Map Noise = 0.192

J1238.2+2613

Peak Flux = 13.74   Map Noise = 0.111

J1238.8+3559

Peak Flux = 1.321   Map Noise = 0.086

J1243.7+2830

Peak Flux = 0.640   Map Noise = 0.109

J1248.2+2747

Peak Flux = 1.227   Map Noise = 0.162

J1249.7+3408

Peak Flux = 30.09   Map Noise = 0.176

J1250.4+2941

Peak Flux = 0.654   Map Noise = 0.097

Note: Peak flux and map noise values are given in mJy/beam.
Contours begin at 2.5 times the map noise level and increase by factors of sqrt(2).

FIG. 11.—Images of the 11 detections from the 18 USS sources observed with the VLA A configuration at 1.4 GHz. The remaining seven are diffuse enough to be resolved out at this resolution of roughly 1″.4.

429

J1249.0+3615.—FIRST shows a roughly $10''$ FR I morphology. This is likely to be a high-*z* CHR or FRG.

J1249.7+3408.—Unresolved in FIRST but a fit to the A configuration map shows a source size of about $0\rlap{.}''8$. This is likely a HzRG.

J1250.4+2941.—FIRST shows a $20''$ FR I morphology, which is mostly resolved out in A configuration. This is likely to be a HzRG or FRG.

J1252.7+2207.—FIRST shows a $20''$ diffuse blob. This is likely to be a high-*z* CHR, HzRG, or FRG.

J1253.4+2703.—FIRST shows a very diffuse object of about $40''$ diameter that is resolved out in A configuration. This is an ideal CHR candidate, though no nearby clusters are known.

J1253.6+2509.—No FIRST or NVSS counterpart.

J1256.9+2811.—FIRST shows a $15''$ FR I morphology. This is likely to be a high-*z* CHR, HzRG, or FRG.

6. CONCLUSIONS AND FUTURE PLANS

We have completed a deep, high-resolution survey at 74 MHz and identified 949 sources. We measured the differential source counts between roughly 0.22 and 11 Jy and found them consistent with those found at 327 MHz (Wieringa 1991) adjusted by a spectral index of roughly $-0.75 < \alpha < -0.5$. Comparison with the 1.4 GHz surveys NVSS and FIRST shows that the average source in our survey is steeper than this. This could be explained if a significant fraction of sources become flat or inverted between 327 and 74 MHz, and so are selected against by our flux limited survey. We find that fainter sources tend to have slightly flatter spectra. Source size studies with the FIRST survey indicate that the flat spectrum objects are much smaller than the steeper spectrum objects on average.

A small fraction of sources, 26 out of 949, qualify as USS sources with spectral indices steeper than $\alpha < -1.2$. We present a list of these sources, along with FIRST images of 24 of these and higher resolution A configuration VLA images of 18 USS sources. We find that all but a few of these are good candidates for high-redshift radio galaxies, while the others are probably fossil radio galaxies or cluster halo, relic systems. We plan optical and spectroscopic follow-up on the HzRG candidates to measure their redshifts.

REFERENCES

Archibald, E. N., Dunlop, J. S., Hughes, D. H., Rawlings, S., Eales, S. A., & Ivison, R. J. 2001, MNRAS, 323, 417

Bettoni, D., Falomo, R., Fasano, G., & Govoni, F. 2003, A&A, 399, 869

Blundell, K. M., Rawlings, S., Eales, S. A., Taylor, G., & Bradley, A. D. 1998, MNRAS, 295, 265

Blundell, K. M., Rawlings, S., & Willott, C. J. 1999, AJ, 117, 677

Carilli, C. L., Roettgering, H. J. A., van Ojik, R., Miley, G. K., & van Breugel, W. J. M. 1997, ApJS, 109, 1

Chambers, K. C., Miley, G. K., van Breugel, W. J. M., & Huang, J.-S. 1996, ApJS, 106, 215

Condon, J. J., Cotton, W. D., Greisen, E. W., Yin, Q. F., Perley, R. A., Taylor, G. B., & Broderick, J. J. 1998, AJ, 115, 1693

Cornwell, T. J., & Perley, R. A. 1992, A&A, 261, 353

Cotton, W. D., & Condon, J. J. 2002, URSI General Assembly, paper 0944 (Maastricht: URSI), 1

Cuby, J.-G., Le Fèvre, O., McCracken, H., Cuillandre, J.-C., Magnier, E., & Meneux, B. 2003, A&A, 405, L19

De Breuck, C., van Breugel, W., Röttgering, H. J. A., & Miley, G. 2000, A&AS, 143, 303

De Breuck, C., van Breugel, W., Stanford, S. A., Röttgering, H., Miley, G., & Stern, D. 2002, AJ, 123, 637

Dunlop, J. S., McLure, R. J., Kukula, M. J., Baum, S. A., O'Dea, C. P., & Hughes, D. H. 2003, MNRAS, 340, 1095

Enßlin, T. A., & Röttgering, H. 2002, A&A, 396, 83

Gower, J. F. R., Scott, P. F., & Wills, D. 1967, MmRAS, 71, 49

Hu, E. M., Cowie, L. L., McMahon, R. G., Capak, P., Iwamuro, F., Kneib, J.-P., Maihara, T., & Motohara, K. 2002, ApJ, 568, L75

Jarvis, M. J., Rawlings, S., Eales, S., Blundell, K. M., Bunker, A. J., Croft, S., McLure, R. J., & Willott, C. J. 2001, MNRAS, 326, 1585

Kassim, N. E., Lazio, T. J. W., Erickson, W. C., Crane, P. C., Perley, R. A., & Hicks, B. 2000, Proc. SPIE, 4015, 328

Kassim, N. E., Perley, R. A., Erickson, W. C., & Dwarakanath, K. S. 1993, AJ, 106, 2218

Kassim, N. E., et al. 2004, ApJS, submitted

Kodaira, K., et al. 2003, PASJ, 55, L17

Magorrian, J., et al. 1998, AJ, 115, 2285

Overzier, R. A., Röttgering, H. J. A., Rengelink, R. B., & Wilman, R. J. 2003, A&A, 405, 53

Pilkington, J. D. H., & Scott, P. F. 1965, MmRAS, 69, 183

Rawlings, S., Lacy, M., Blundell, K. M., Eales, S. A., Bunker, A. J., & Garrington, S. T. 1996, Nature, 383, 502

Rengelink, R. B., Tang, Y., de Bruyn, A. G., Miley, G. K., Bremer, M. N., Roettgering, H. J. A., & Bremer, M. A. R. 1997, A&AS, 124, 259

Reuland, M. R., Röttgering, H., & van Breugel, W. 2003, New A Rev., 47, 303

Röttgering, H. J. A., Lacy, M., Miley, G. K., Chambers, K. C., & Saunders, R. 1994, A&AS, 108, 79

Steidel, C. C., Adelberger, K. L., Giavalisco, M., Dickinson, M., & Pettini, M. 1999, ApJ, 519, 1

Steidel, C. C., Giavalisco, M., Pettini, M., Dickinson, M., & Adelberger, K. L. 1996, ApJ, 462, L17

van Breugel, W., De Breuck, C., Stanford, S. A., Stern, D., Röttgering, H., & Miley, G. 1999, ApJ, 518, L61

Verkhodanov, O. V., Trushkin, S. A., Andernach, H., & Chernenkov, V. N. 1997, in ASP Conf. Ser. 125, Astronomical Data Analysis Software and Systems VI, ed. ed. G. Hunt & H. E. Payne (San Francisco: ASP), 322

Wall, J. V., & Jackson, C. A. 1997, MNRAS, 290, L17

White, R. L., Becker, R. H., Helfand, D. J., & Gregg, M. D. 1997, ApJ, 475, 479

Wieringa, M. H. 1991, Ph.D. thesis, Leiden Univ.

Willott, C. J., Rawlings, S., Jarvis, M. J., & Blundell, K. M. 2003, MNRAS, 339, 173